

# Detection of hydrogen sulphide above the clouds in Uranus' atmosphere

Patrick G. J. Irwin<sup>1</sup>, Daniel Toledo<sup>1</sup>, Ryan Garland<sup>1</sup>, Nicholas A. Teanby<sup>2</sup>, Leigh N. Fletcher<sup>3</sup>, Glenn A. Orton<sup>4</sup>, & Bruno Bézard<sup>5</sup>

<sup>1</sup>*Department of Physics (Atmospheric, Oceanic and Planetary Physics), University of Oxford, Parks Rd, Oxford, OX1 3PU, UK.*

<sup>2</sup>*School of Earth Sciences, University of Bristol, Wills Memorial Building, Queens Road, Bristol, BS8 1RJ, UK.*

<sup>3</sup>*Department of Physics & Astronomy, University of Leicester, University Road, Leicester, LE1 7RH, UK.*

<sup>4</sup>*Jet Propulsion Laboratory, California Institute of Technology, 4800 Oak Grove Drive, Pasadena, CA 91109, USA*

<sup>5</sup>*LESIA, Observatoire de Paris, PSL Research University, CNRS, Sorbonne Universités, UPMC Univ. Paris 6, Université Paris-Diderot, Sorbonne Paris Cité, 5 place Jules Janssen, 92195 Meudon, France.*

**Visible to near-infrared observations indicate that the cloud top of the main cloud deck on Uranus lies at a pressure level of between 1.2 and 3 bar. However, its composition has never been unambiguously identified, although it is widely assumed to be composed primarily of either ammonia (NH<sub>3</sub>) or hydrogen sulphide (H<sub>2</sub>S) ice. Here we present evidence of a clear detection of gaseous H<sub>2</sub>S above this cloud deck in the wavelength region 1.57 – 1.59 μm**

21 **with a mole fraction of 0.4 – 0.8 ppm at the cloud top. Its detection constrains the deep**  
22 **bulk sulphur/nitrogen abundance to exceed 4.4 – 5.0 times the solar value in Uranus’ bulk**  
23 **atmosphere, and places a lower limit on the mole fraction of H<sub>2</sub>S below the observed cloud**  
24 **of  $(1.0 – 2.5) \times 10^{-5}$ . The detection of gaseous H<sub>2</sub>S at these pressure levels adds to the weight**  
25 **of evidence that the principal constituent of 1.2 – 3-bar cloud is likely to be H<sub>2</sub>S ice.**

26 **Introduction** In the absence of any spectrally identifiable ice absorption features, the identity of  
27 the main component of the cloud in Uranus’ atmosphere with cloud top pressure 1.2 – 3 bar<sup>1-3</sup>  
28 has long been a source of debate. The assumption that it is composed of either ammonia (NH<sub>3</sub>)  
29 or hydrogen sulphide (H<sub>2</sub>S) ice<sup>3</sup> is based on the expected presence at deeper pressures ( $\sim$  40 bar)  
30 of an ammonium hydrosulphide (NH<sub>4</sub>SH) cloud. This cloud combines together in equal parts  
31 any available H<sub>2</sub>S and NH<sub>3</sub>, leaving the remaining more abundant molecule to condense alone at  
32 lower pressures<sup>4</sup>. Deeper in the atmosphere (20 – 40 bar), observations of Uranus and Neptune  
33 at microwave wavelengths (1 – 20 cm) with the Very Large Array (VLA)<sup>5</sup> found that there was a  
34 missing component of continuum absorption, which was concluded to be likely due to the pressure-  
35 broadened wings of H<sub>2</sub>S lines with wavelengths of less than a few mm. The deep abundance of  
36 H<sub>2</sub>S was estimated to be 10 – 30 $\times$  solar and this analysis further concluded, building upon previous  
37 studies<sup>6,7</sup>, that the bulk S/N ratio must exceed  $\sim$  5 $\times$  the assumed solar ratio<sup>8</sup> in order that the  
38 bulk abundance of H<sub>2</sub>S exceeds that of NH<sub>3</sub>, leaving residual H<sub>2</sub>S above the deeper NH<sub>4</sub>SH cloud.  
39 Hydrogen sulphide is believed to be a significant component of all the giant planet atmospheres and  
40 has been detected *in situ* in Jupiter’s deep atmosphere by the Galileo probe mass spectrometer<sup>9</sup> (and  
41 also in comets, both *in situ* and remotely<sup>10,11</sup>). However, it has never been unambiguously remotely

42 detected in the atmospheres of any of the giant planets, aside from a possible debated detection in  
43 Jupiter’s atmosphere following the impact of Comet Shoemaker-Levy 9 in 1994<sup>12,13</sup>. Hence, while  
44 H<sub>2</sub>S is probably the source of the missing continuum absorption at microwave wavelengths in  
45 Uranus and Neptune’s atmospheres, and is also probably the main component of the 1.2 – 3-bar  
46 cloud, it has never been unequivocally detected in Uranus’ atmosphere to confirm this.

47       Detection of H<sub>2</sub>S and NH<sub>3</sub> absorption features at thermal-IR wavelengths is very challenging  
48 due to the extremely cold atmospheric temperatures in Uranus’ atmosphere, but at visible/near-  
49 infrared wavelengths, there are weak absorption bands that could potentially be detected in sunlight  
50 reflected from the cloud tops at wavelengths where the absorption of other gases is weak. The  
51 available line data for the key condensable volatiles in Uranus’ atmosphere (i.e. CH<sub>4</sub>, NH<sub>3</sub>, H<sub>2</sub>S)  
52 have recently been greatly improved<sup>14,15</sup> and, although these absorptions are weak, we looked to  
53 see whether we could detect these features in near-IR ground-based high resolution spectroscopic  
54 measurements.

55 **Observations** Observations of Uranus (with adaptive optics) were made with Gemini-North’s  
56 Near-infrared Integral Field Spectrometer (NIFS) instrument in 2009/2010<sup>16,17</sup>. NIFS records 3'' ×  
57 3'' image ‘cubes’ with a pixel size of 0.103 × 0.043'', where each pixel is a spectrum covering, in  
58 the H-band, the wavelength range 1.476 – 1.803 μm with a spectral resolution of R = 5290. For  
59 this study we used observations recorded on 2nd November 2010 at approximately 06:00UT<sup>17</sup>. To  
60 minimise random noise we averaged the observations over seven 5 × 5 pixel boxes, indicated in  
61 Fig. 1 and listed in Table 1. We selected the wavelength region 1.49 – 1.64 μm for our analysis,

62 comprising  $n_y = 937$  spectral points. We initially set the noise at each wavelength to be the stan-  
63 dard deviation of the data in these  $5 \times 5$  pixel boxes. However, we found that we were not quite  
64 able to fit these spectra to a precision of  $\chi^2/n_y \sim 1$  and attributed this to unknown deficiencies  
65 in our spectral modelling. We thus multiplied these errors by a single factor of 1.6 at all wave-  
66 lengths (except for area ‘6’, for which the variance was already sufficiently large) to account for  
67 these ‘forward-modelling’ errors. For our reference spectrum we chose the region close to the disc  
68 centre, centred at  $15.3^\circ\text{N}$  (Area ‘1’), but performed the same analysis for all other selected regions,  
69 reported in the supplementary material.

70 **Analysis** To model the observed spectra we used the NEMESIS<sup>18</sup> retrieval model, using the  
71 correlated-k approximation with ‘k’-tables generated from the recently published WKLMC@80K+<sup>14</sup>  
72 line data for  $\text{CH}_4$  and updated line data for  $\text{H}_2\text{S}$  and  $\text{NH}_3$  from HITRAN2012<sup>15</sup>. The mean absorp-  
73 tion strengths of  $\text{CH}_4$ ,  $\text{NH}_3$  and  $\text{H}_2\text{S}$  across the H-band wavelength range contained in these data  
74 (calculated at 100 K and 1 atm) are shown in Fig. 1. Our *a priori* vertical atmospheric profile was  
75 based on the ‘F1’ temperature profile, determined from HST/STIS and Voyager 2 observations<sup>3</sup>.  
76 This profile has a deep methane mole fraction of 4%<sup>19</sup>, and has a varying relative humidity with  
77 height above the condensation level. The He: $\text{H}_2$  ratio was set to 0.131 and the profile includes  
78 0.04% mole fraction of Ne<sup>3</sup>. To this profile we added  $\text{NH}_3$  and  $\text{H}_2\text{S}$ , assuming arbitrary ‘deep’  
79 mole fractions (i.e. above the putative  $\text{NH}_4\text{SH}$  cloud) of 0.1% for both, and limited their abun-  
80 dance to not exceed the saturated vapour pressure<sup>20</sup> in the troposphere as the temperature falls with  
81 height, adjusting the abundance of hydrogen and helium (keeping He: $\text{H}_2$  = 0.131) to ensure the  
82 mole fractions summed to unity at each pressure level. Figure 2 shows the modelled abundance

83 profiles of the three condensible species falling with height. We can see that the saturated vapour  
84 pressure of H<sub>2</sub>S at the pressure of the main clouds of Uranus (1.2 – 3 bar) is approximately 2000  
85 times higher than that of NH<sub>3</sub>. Hence, even though the peak NH<sub>3</sub> absorption strength in this spec-  
86 tral region is, from Fig. 1, ~ 100 times stronger than that of H<sub>2</sub>S, we expect the absorption lines  
87 of H<sub>2</sub>S to be far more visible due to the higher likely abundance of H<sub>2</sub>S and also the lines of H<sub>2</sub>S  
88 having maximum strength at wavelengths of minimum methane opacity (Fig. 1). The very low  
89 saturated vapour pressure of NH<sub>3</sub> at the 1.2–3 bar level in Uranus’ atmosphere makes it likely that  
90 NH<sub>3</sub> would not have enough abundance to condense into a cloud with sufficient opacity at this  
91 level as has previously been noted<sup>3</sup>.

92 We fitted the spectrum using a multiple-scattering model and modelled cloud opacity with  
93 a vertically continuous profile of particles (at 39 levels) with a Gamma size distribution of mean  
94 radius 1.0  $\mu\text{m}$  and variance 0.05. This size distribution is typical of that assumed in previous  
95 analyses<sup>2,21</sup>, but is an assumption and is not constrained by, for example, a microphysical model.  
96 In addition, the assumption that the particles have the same size distribution at all altitudes is  
97 an oversimplification since we would expect that in real clouds the particles would be smaller at  
98 higher altitudes. However, the primary objective of this study was to search for the spectral sig-  
99 nature of H<sub>2</sub>S gas, rather than to fit a sophisticated cloud model and we thus chose a model that  
100 would be simple and easy to fit. It should be noted that our simple cloud model is used to model  
101 not only the effects of the main 1.2 – 3 bar cloud, but also any CH<sub>4</sub> cloud opacity and any tropo-  
102 spheric/stratospheric haze opacity that may be present. In addition to fitting the cloud opacity at  
103 each level in the atmosphere, we also fitted the imaginary refractive index spectrum of the parti-

cles (assumed to be the same at all vertical levels) at nine wavelengths between 1.4 and 1.8  $\mu\text{m}$ ,  
reconstructing the real part of the refractive index spectrum using the Kramers-Kronig relation<sup>21</sup>,  
assuming  $n_{real} = 1.4$  at 1.6  $\mu\text{m}$ . We constrained the imaginary refractive index spectrum to vary  
reasonably slowly with wavelength, to avoid degeneracy with the H<sub>2</sub>S signal we were trying to de-  
tect (see Methods). Self-consistent extinction cross-sections, single-scattering albedos and phase  
functions were then computed at all wavelengths using Mie theory, with the phase functions ap-  
proximated with Henyey-Greenstein functions (see Methods section). The total number of variable  
parameters in our retrieval was thus  $n_x = 39 + 9 = 48$ , and thus the total number of degrees of  
freedom,  $n = n_y - n_x$  was 889.

**Results** Figure 3 shows our fit to the reference Uranus spectrum (Area ‘1’ of Fig. 1 and Table 1)  
when H<sub>2</sub>S and NH<sub>3</sub> absorption is neglected, using three different *a priori* values of the imaginary  
refractive index of 0.001, 0.01 and 0.1, respectively, at all wavelengths with an *a priori* error  
of  $\pm 50\%$ . We can see that reasonably good fits are achieved for all three cases, but that better  
fits are achieved with higher *a priori* values, with similar results for  $n_i = 0.01$  and  $n_i = 0.1$   
( $\chi^2/n \sim 1.7$ ). For the  $n_i = 0.001$  case, a poorer fit is achieved ( $\chi^2/n \sim 1.9$ ) as the solution cannot  
move far enough away from the *a priori* to properly fit the spectrum. As a result the retrieved  
particles have low imaginary refractive index and so are more scattering, necessitating the cloud  
profile opacity to reduce quickly at pressures greater than 2–3 bar to prevent significant reflection  
from these levels. This is in stark contrast to the other two solutions, where  $n_i$  is much higher  
( $n_i \sim 0.06$ ), and where we find that the single-scattering albedo of the particles is  $\varpi = 0.7–0.8$  and  
phase function asymmetry is  $g \sim 0.7$  across the observed spectral range (Supplementary Fig.1).

125 These retrieved single-scattering albedo and phase-function asymmetry values agree very well  
126 with a limb-darkening analysis<sup>16</sup>, which used these same Gemini/NIFS data smoothed to a lower  
127 resolution of FWHM = 0.004  $\mu\text{m}$  and older, lower-resolution methane absorption k-distribution  
128 data<sup>22</sup>, and also with an analysis of Keck and HST images<sup>23</sup>, which recommended  $\varpi = 0.75$  and  
129  $g = 0.7$ . An important consequence of the low single-scattering albedo of the retrieved particles is  
130 that solar photons are quickly absorbed as they reach the cloud tops and so we do not see significant  
131 reflection from particles residing at pressures greater than 2–3 bar. This can be seen in the retrieved  
132 error bars for the cloud opacity profiles in Fig. 3 quickly relaxing back to their *a priori* value as  
133 the pressure increases and the profiles for the higher  $n_i$  values tending smoothly back to their *a*  
134 *priori* opacity/bar values. As a result, although we can clearly detect the cloud-top pressure at these  
135 wavelengths, we cannot tell where the base is and thus cannot differentiate between a vertically  
136 thin cloud based at 2–3 bar, or a cloud that extends vertically down to several bars with the same  
137 cloud-top pressure. We also note here that when the particles are constrained to be more scattering,  
138 the peak of cloud opacity is at a lower pressure than for the case with more absorbing particles.  
139 This phenomenon may help to explain why HST/STIS<sup>3</sup> retrievals, which assume the particles to  
140 be more scattering, find the cloud tops to be at lower pressures (1.2 bar) than retrievals near 1.5  
141  $\mu\text{m}$ <sup>1,2</sup>, which assume more absorbing particles and find cloud tops at 2–3-bar.

142 Figure 4 compares our best fits to the observed reference spectrum (Area ‘1’ at 15.3°N) in  
143 the 1.56 – 1.60  $\mu\text{m}$  region, including or excluding H<sub>2</sub>S absorption. When H<sub>2</sub>S absorption is not in-  
144 cluded, we find that there is a significant discrepancy between the measured and modelled spectra,  
145 giving  $\chi^2/n = 1.71$ . This discrepancy is significantly reduced when H<sub>2</sub>S absorption is included and

146 NEMESIS allowed to scale the abundance of H<sub>2</sub>S, achieving a much closer fit with  $\chi^2/n = 1.30$ .  
147 When H<sub>2</sub>S absorption is not included, there are several peaks in the difference spectrum (Fig. 4)  
148 that match perfectly the effect of including or excluding this gas in the spectral calculation. We ex-  
149 amined the correlation between the expected H<sub>2</sub>S signal and this difference spectrum between 1.57  
150 and 1.60  $\mu\text{m}$ , and found a Pearson correlation coefficient of 0.718 (indicating a strong correlation)  
151 and a Spearman rank correlation coefficient of 0.602, with a two-sided significance value of  $D =$   
152  $6.88 \times 10^{-20}$ , which equates to a 9- $\sigma$ -level detection. We also tested the effect on the calculated  
153 spectrum of including or excluding 100% relative humidity of ammonia (NH<sub>3</sub>), but found that this  
154 was completely undetectable due to ammonia's extremely low abundances at these temperatures.  
155 In case the ammonia abundance in Uranus' atmosphere is in reality highly supersaturated, we also  
156 tested the effect on the calculated spectrum of supersaturating NH<sub>3</sub> by factor of 1000, also shown  
157 in Fig. 4. However, we found that the absorption features of NH<sub>3</sub> do not coincide at all well with  
158 the difference spectrum, with correlation coefficients of only 0.271 (Pearson) and 0.256 (Spear-  
159 man), respectively. We thus conclude that NH<sub>3</sub> is not the source of the missing absorption. The  
160 correlation between the spectral discrepancy of the fit, when H<sub>2</sub>S is neglected, and the differences  
161 between the modelled spectra when H<sub>2</sub>S or NH<sub>3</sub> absorption is added are shown in Supplementary  
162 Fig. 2.

163 The retrieved relative humidity of the H<sub>2</sub>S profile needed to match the observed absorption  
164 features was  $113 \pm 12\%$ . Since the mole fraction of H<sub>2</sub>S decreases rapidly with height, this scaling  
165 factor is strongly weighted by the abundance of H<sub>2</sub>S just above the cloud tops, i.e. at 2–3 bar and  
166 found to be 0.47 ppm, but is consistent with the H<sub>2</sub>S profile having 100% relative humidity in this

167 region. However, this conclusion depends upon both the assumed temperature profile, which sets  
168 the saturated vapour pressure, and also the assumed methane profile, which affects the retrieved  
169 cloud-top pressure and thus the peak pressure level (and thus local temperature) of sensitivity  
170 to H<sub>2</sub>S. To test these effects we repeated our retrievals using a vertical profile of temperature  
171 and abundance estimated from Spitzer<sup>24</sup>, which has a lower CH<sub>4</sub> abundance of 3.2%, compared  
172 with 4% for the ‘F1’ profile<sup>3</sup>, but is slightly warmer at pressures greater than 1 bar, resulting in  
173 higher saturated vapour pressures of H<sub>2</sub>S. As might be expected, the lower CH<sub>4</sub> abundance of this  
174 profile led to the retrieved cloud opacity peaking at slightly higher pressures to achieve the required  
175 column abundance of CH<sub>4</sub> (Table 1) and the retrieved H<sub>2</sub>S relative humidity at the deeper cloud  
176 tops in the warmer atmosphere was only  $16 \pm 2\%$ . Since it is not clear which of these two profiles is  
177 more reliable, (although the ‘F1’ profile was found to be inconsistent with Spitzer observations<sup>24</sup>) it  
178 can be seen that although we clearly detect the presence of H<sub>2</sub>S at Uranus’ cloud tops, it is difficult  
179 to quantitatively determine its relative humidity. However, we can see from Table 1 that there is  
180 very good correspondence between the retrieved values of column abundance of H<sub>2</sub>S above the  
181 clouds for the two temperature profiles and also between the retrieved mole fraction of H<sub>2</sub>S at the  
182 cloud-top pressure level of  $(4.7 \pm 0.5) \times 10^{-7}$  for the ‘F1’ profile and  $(4.3 \pm 0.5) \times 10^{-7}$  for the  
183 Spitzer profile, where we have propagated the relative humidity retrieval errors.

184 Table 1 and Supplementary Figs. 3 – 11 show our fits at the other test points on Uranus’  
185 disc, indicated in Fig. 1. At all locations except in Uranus’ northern polar ‘cap’ feature we found  
186 a clear improvement in our fit to the spectra when H<sub>2</sub>S absorption is included, indicating the  
187 presence of H<sub>2</sub>S at the cloud tops (Table 1), with well defined column abundances above the cloud

188 of  $(2 - 5) \times 10^{19}$  molecule  $\text{cm}^{-2}$  and cloud-top mole fractions of 0.4 – 0.8 ppm. All but one of the  
189 chosen points were on the central meridian, to keep the zenith angle as low as possible to minimise  
190 the computation time of our multiple scattering code, which uses more Fourier components in the  
191 azimuth decomposition direction as the zenith angle increases to maintain accuracy. However,  
192 point ‘2’ was chosen to be at roughly the same latitude as our reference area, but off the central  
193 meridian and closer to the limb to check that our retrieval was robust against zenith angle changes,  
194 which was found to be the case. The absence of a clear  $\text{H}_2\text{S}$  signature near Uranus’ north pole  
195 seems to indicate lower  $\text{H}_2\text{S}$  above the clouds in this region, in the same way that microwave  
196 observations found that the polar regions were depleted in microwave absorbers ( $\text{H}_2\text{S}$  and  $\text{NH}_3$ )  
197 at depth<sup>6</sup>. The abundance of methane above the clouds is also known to be reduced at these  
198 latitudes<sup>3,19</sup>. Alternatively, it could also be that the  $\text{H}_2\text{S}$  signal is masked by increased abundance  
199 of tropospheric haze, but Table 1, which lists a haze ‘index’, given by the observed radiance in a  
200 methane absorbing band divided by the radiance at continuum wavelengths, does not suggest that  
201 the polar region is particularly affected by overlying haze. However, to explore this further requires  
202 a detailed examination of spectra in the polar regions, which is beyond the scope of this paper.

203 **Discussion** If we could be sure that the main observed cloud deck was vertically thin and com-  
204 posed of  $\text{H}_2\text{S}$  ice, then we could constrain the abundance of  $\text{H}_2\text{S}$  below it by equating the cloud  
205 base to the condensation level. However, the low retrieved single-scattering albedo of the cloud  
206 particles means that we cannot tell between whether we are seeing a vertically thin cloud based  
207 at 2–3 bar or just the top of a vertically extended cloud that extends to several bars. Instead, our  
208 detection of  $\text{H}_2\text{S}$  can be used to give a lower limit on its abundance below the observed cloud.

209 Assuming the main cloud is made of H<sub>2</sub>S ice, is vertically thin and is based at 3 bars, and that the  
 210 STIS/Voyager-2 ‘F1’ temperature profile<sup>3</sup> we have assumed is correct, the saturated mole fraction  
 211 of H<sub>2</sub>S at the 3-bar level (where the temperature is 116.1K) is estimated to be  $1.1 \times 10^{-5}$ . Alterna-  
 212 tively, using the Spitzer profile<sup>24</sup>, the saturated vapour mole fraction at the 3-bar level (where the  
 213 temperature is 119.5 K) is  $2.5 \times 10^{-5}$ . Hence, we can conclude that the mole fraction of H<sub>2</sub>S at  
 214 pressures > 3 bar, immediately below the clouds must be >  $(1.0 - 2.5) \times 10^{-5}$ . We can compare  
 215 this with the expected abundances of H<sub>2</sub>S and NH<sub>3</sub> from microwave VLA studies<sup>5-7</sup>, who found  
 216 the abundance of H<sub>2</sub>S to be  $10 - 30 \times$  solar, and S/N >  $\sim 5$ , assuming solar abundances<sup>8</sup> of  
 217  $\text{H}_2\text{S}/\text{H}_2 = 3.76 \times 10^{-5}$  and  $\text{NH}_3/\text{H}_2 = 1.74 \times 10^{-4}$  (giving N/S = 4.6). Using these values,  $10 \times$  solar  
 218 H<sub>2</sub>S and  $2 \times$  solar NH<sub>3</sub> would give a residual mole fraction of H<sub>2</sub>S above a deeper NH<sub>4</sub>SH cloud  
 219 of at least  $3 \times 10^{-5}$ , while for  $30 \times$  solar H<sub>2</sub>S and  $6 \times$  solar NH<sub>3</sub>, the expected residual H<sub>2</sub>S mole  
 220 fraction increases to  $9 \times 10^{-5}$ . Both these values are significantly greater than our estimated mini-  
 221 mum residual abundance, but are consistent with it and may suggest that the base of the cloud lies  
 222 at pressures greater than 3 bar. A more recent analysis of Spitzer Uranus observations<sup>24</sup> suggests  
 223 a residual H<sub>2</sub>S mole fraction of  $1.5 \times 10^{-5}$  in order to reconcile the millimetre spectrum with the  
 224 temperature profile derived from Spitzer, which is much closer to our estimate. Interpolating to  
 225 the pressure levels in our assumed ‘F1’ temperature-pressure profile<sup>3</sup> where the VLA and Spitzer  
 226 estimates of residual H<sub>2</sub>S abundance are equal to the saturated vapour pressure abundances we  
 227 deduce that the base of the main cloud must lie at a pressure of 3.1 – 4.1 bar. Alternatively, if  
 228 we assume the Spitzer temperature-pressure profile<sup>24</sup>, we find a pressure range 2.8 – 3.7 bar. The  
 229 fact that we detect H<sub>2</sub>S at all at Uranus’ cloud tops confirms that the deep abundance of H<sub>2</sub>S must

230 exceed that of  $\text{NH}_3$  and hence that  $S/N > 4.6 \times$  solar for the solar abundance ratios<sup>8</sup> assumed  
231 by the VLA study<sup>5,6</sup>. We note, however, that there are other, more recent estimates of the solar  
232 abundance ratios, for which the solar N/S value varies from 4.4<sup>25</sup> to 5.0<sup>26</sup>. Hence, to ensure that  
233 the deep abundance of  $\text{H}_2\text{S}$  exceeds that of  $\text{NH}_3$  we conclude that the S/N ratio in Uranus' bulk  
234 atmosphere exceeds  $4.4\text{--}5.0 \times$  solar. The clear detection of gaseous  $\text{H}_2\text{S}$  above Uranus' clouds  
235 leads us to conclude that  $\text{H}_2\text{S}$  ice likely forms a significant component of the main clouds at 1.2  
236 – 3 bar. To our knowledge the imaginary refractive index spectrum of  $\text{H}_2\text{S}$  ice has not been mea-  
237 sured and hence we cannot directly verify if our retrieved refractive index spectrum is consistent  
238 with  $\text{H}_2\text{S}$  ice. However, very large imaginary refractive indices, such as we retrieve, are absent in  
239 the measured complex refractive index spectra of  $\text{H}_2\text{O}$ ,  $\text{CH}_4$  and  $\text{NH}_3$  ices. This suggests that if  
240 Uranus' main clouds are indeed formed primarily of  $\text{H}_2\text{S}$  ice, the particles may not be pure con-  
241 densates, but may be heavily coated or mixed with photochemical products drizzling down from  
242 the stratosphere above, lowering their single-scattering albedos.

## 243 1 References

- 244 1. de Kleer, K., Luszcz-Cook, S., de Pater, I., Ádámkóvics, M. & Hammel, H.B. Clouds and  
245 aerosols on Uranus: Radiative transfer modeling of spatially-resolved near-infrared Keck  
246 spectra. *Icarus* **256**, 120 – 137 (2015).
- 247 2. Irwin, P.G.J., de Bergh, C., Courtin, R., Bézard, B., Teanby, N.A., Davis, G.R., Fletcher, L.N.,  
248 Orton, G.S., Calcutt, S.B., Tice, D. & Hurley, J. The application of new methane line absorp-  
249 tion data to Gemini-N/NIFS and KPNO/FTS observations of Uranus' near-infrared spectrum.  
250

- 251 *Icarus* **220**, 369 – 382 (2012b).
- 252 3. Sromovsky, L.A., Fry, P.M., & Kim, J.H. Methane on Uranus: The case for a compact CH<sub>4</sub>  
253 cloud layer at low latitudes and a severe CH<sub>4</sub> depletion at high latitudes based on a re-analysis  
254 of Voyager occultation measurements and STIS spectroscopy. *Icarus* **215**, 292 – 312 (2011).
- 255 4. Weidenschilling, S.J. & Lewis, J.S. Atmospheric and cloud structures of the Jovian planets.  
256 *Icarus* **20**, 465 – 76 (1973).
- 257 5. de Pater, I., Romani, P.N. & Atreya, S.K. Possible microwave absorption by H<sub>2</sub>S gas in Uranus’  
258 and Neptune’s atmospheres. *Icarus* **91**, 220 – 233 (1991).
- 259 6. de Pater, I., Romani, P.N. & Atreya, S.K. Uranus’ deep atmosphere revealed. *Icarus* **82**, 288 –  
260 313 (1989).
- 261 7. de Pater, I. & Massie, S. Models of the millimeter-centimeter spectra of the giant planets.  
262 *Icarus* **62**, 143 – 171 (1985).
- 263 8. Cameron, A.G.W. Elemental and Nuclidic Abundances in the Solar System. In *Essays in*  
264 *Nuclear Astrophysics* (C. A. Barnes, D. D. Clayton, and D. N. Schramm, Eds.), pp. 23-43,  
265 Cambridge Univ. Press, London/New York (1982).
- 266 9. Niemann, H.B., et al. The composition of the jovian atmosphere as determined by the Galileo  
267 probe mass spectrometer. *J. Geophys. Res.* **103**, 22831 – 22845 (1998).

- 268 10. Boissier, J., Bockelée-Morvan, Biver, N., Crovisier, J., Despois, D., Marsden, B.G. & Moreno,  
269 R. Interferometric imaging of the sulfur-bearing molecules H<sub>2</sub>S, SO and CS in comet C/1995  
270 O1 (Hale-Bopp). *Astron. Astrophys.* **475**, 1131 – 1144 (2007).
- 271 11. Eberhardt, P., Meier, R., Krankowsky, D. & Hodges, P.R. Methanol and hydrogen sulfide in  
272 comet P/Halley. *Astron. Astrophys.* **288**, 315 – 329 (1994).
- 273 12. Noll, K.S., McGrath, M.A., Trafton, L.M., Atreya, S.K., Caldwell, J.J., Weaver, H.A., Yelle,  
274 R.V., Barnet, C. & Edgington, S. HST Spectroscopic observations of Jupiter after the collision  
275 of Comet Shoemaker-Levy 9. *Science* **267**, 1307 – 1313 (1995).
- 276 13. Lellouch, E. Chemistry induced by the impacts: Observations. IAU Colloquium 156; *Pro-*  
277 *ceedings of the Space Telescope Science Institute Workshop*, held in Baltimore, Maryland,  
278 May 9–12, 1995. Eds.: Keith S. Noll, Harold A. Weaver, Paul D. Feldman, Cambridge Uni-  
279 versity Press, p. 213 (1996).
- 280 14. Campargue, A., Leshchishina, O., Wang, L., Mondelain, D. & Kassi, S. The WKLMC em-  
281 pirical line lists (5852 – 7919 cm<sup>-1</sup>) for methane between 80 K and 296 K: “Final” lists for  
282 atmospheric and planetary applications. *J. Molec. Spectrosc.* **291**, 16 – 22 (2013).
- 283 15. Rothman, L.S., Gordon, I.E., Babikov, Y., Barbe, A., Benner, D.C., Bernath, P.F., et al. The  
284 HITRAN2012 molecular spectroscopic database, *J.Q.S.R.T.* **130**, 4 – 50 (2013).
- 285 16. Irwin, P.G.J., Teanby, N.A., Davis, G.R., Fletcher, L.N., Orton, G.S., Tice, D. & Kyffin, A.  
286 Uranus’ cloud structure and seasonal variability from Gemini-North and UKIRT observations.  
287 *Icarus* **212**, 339 – 350 (2011).

- 288 17. Irwin, P.G.J., Teanby, N.A., Davis, G.R., Fletcher, L.N., Orton, G.S., Calcutt, S.B., Tice, D.  
289 & Hurley, J. Further seasonal changes in Uranus' cloud structure observed by Gemini-North  
290 and UKIRT. *Icarus* **218**, 47 – 55 (2012a).
- 291 18. Irwin, P.G.J., Teanby, N.A., de Kok, R., Fletcher, L.N., Howett, C.J.A., Tsang, C.C.C., Wil-  
292 son, C.F., Calcutt, S.B., Nixon, C.A. & Parrish, P.D. The NEMESIS planetary atmosphere  
293 radiative transfer and retrieval tool. *J.Q.S.R.T.* **109**, 1136 – 1150 (2008).
- 294 19. Karkoschka, E. & Tomasko, M. The haze and methane distributions on Uranus from HST-STIS  
295 spectroscopy. *Icarus* **202**, 287–309 (2009).
- 296 20. Fray, N. & Schmitt, B. Sublimation of ices of astrophysical interest: A bibliographic review.  
297 *Plan. Space. Sci.* **57**, 2053 – 2080 (2009).
- 298 21. Irwin, P.G.J., Tice, D.S., Fletcher, L.N., Barstow, J.K., Teanby, N.A., Orton, G.S. & Davis,  
299 G.R. Reanalysis of Uranus' cloud scattering properties from IRTF/SpeX observations using a  
300 self-consistent scattering cloud retrieval scheme. *Icarus* **250**, 462 – 476 (2015).
- 301 22. Karkoschka, E. & Tomasko, M. Methane absorption coefficients for the jovian planets from  
302 laboratory, Huygens, and HST data. *Icarus* **205**, 674 – 694 (2010).
- 303 23. Sromovsky, L.A. & Fry, P.M. Spatially resolved cloud structure on Uranus: Implications of  
304 near-IR adaptive optics imaging. *Icarus* **192**, 527 – 557 (2007).
- 305 24. Orton, G.S., Fletcher, L.N., Moses, J.I., Mainzer, A., Hines, D., Hammel, H., Martin-Torres,  
306 J., Burgdorf, M., Merlet, C. & Line, M.R. 1. Mid-Infrared spectroscopy of Uranus from the

307 Spitzer Infrared Spectrometer: Determination of the mean temperature of the upper tropo-  
308 sphere and stratosphere. *Icarus* **243**, 494 – 513 (2014).

309 25. Grevesse, N., Asplund, M. & Sauval, A.D. The solar chemical composition. *Space Sci. Rev.*  
310 **130**, 105 – 114 (2007).

311 26. Lodders. K. Solar System Abundances of the Elements, in *Principles and Perspectives in*  
312 *Cosmochemistry*, Astrophysics and Space Science Proceedings, ISBN 978-3-642-10351-3.  
313 Springer-Verlag Berlin Heidelberg, p. 379 (2010).

314 **Correspondence** Correspondence and requests for materials should be addressed to Patrick G. J. Irwin  
315 (email: patrick.irwin@physics.ox.ac.uk).

316 **Acknowledgements** We are grateful to the United Kingdom Science and Technology Facilities Council  
317 for funding this research and also to our support astronomers: Richard McDermid and Chad Trujillo (2009,  
318 2010). The Gemini Observatory is operated by the Association of Universities for Research in Astronomy,  
319 Inc., under a cooperative agreement with the NSF on behalf of the Gemini partnership: the National Science  
320 Foundation (United States), the Science and Technology Facilities Council (United Kingdom), the National  
321 Research Council (Canada), CONICYT (Chile), the Australian Research Council (Australia), Ministério da  
322 Ciência e Tecnologia (Brazil) and Ministerio de Ciencia, Tecnología e Innovación Productiva (Argentina).  
323 We thank Larry Sromovsky for providing the code used to generate our Rayleigh-scattering opacities. Glenn  
324 Orton was supported by NASA funding to the Jet Propulsion Laboratory, California Institute of Technology.  
325 Leigh Fletcher was supported by a Royal Society Research Fellowship at the University of Leicester.

326 **Author Contributions** P.G.J.I. wrote the proposal to make the original observations and reduced the data

327 and re-analysed it using the NEMESIS code; B.B. and R.G. assisted in identifying and validating the line  
328 data used. G.A.O. provided the Spitzer T-P profile used. L.N.F., N.A.T., D.T., and all co-authors contributed  
329 to the analysis, interpretation of the results, and all co-wrote the final paper.

330 **Competing Interests** The authors declare that they have no competing financial interests.

## 331 **2 Figure Legends**

332 Figure 1. The appearance and spectrum of Uranus at the near-infrared wavelengths observed by  
333 Gemini/NIFS and associated absorption spectra of CH<sub>4</sub>, NH<sub>3</sub> and H<sub>2</sub>S. Panel A: The appearance  
334 of Uranus at 1.55 μm (low methane absorption, showing reflection for cloud/haze at all vertical  
335 levels), observed with Gemini/NIFS on 2nd November 2010 at approximately 06:00UT, showing  
336 the position of the seven 5 × 5 pixel test areas picked for retrieval analysis. Panel B: The appearance  
337 of Uranus at 1.62 μm (high methane absorption, showing reflection from upper atmospheric haze  
338 only). Panel C: Reference spectrum of Uranus<sup>16</sup> analysed in this study, averaged over area ‘1’ just  
339 north of the equator, near the disc centre, with a mean latitude of 15.3°N, and error estimates shown  
340 in grey. Panel D: Mean strength listed in the k-distribution tables used in this study across the  
341 Gemini/NIFS spectral range. These absorption tables were generated from the WKLMC@80K+<sup>14</sup>  
342 database for CH<sub>4</sub>, and from HITRAN2012<sup>15</sup> for H<sub>2</sub>S and NH<sub>3</sub>. These mean absorption coefficients  
343 have been computed at a temperature of 100 K and pressure of 1 atm, similar to conditions found at  
344 the tops of Uranus’ main visible clouds. Note that for NH<sub>3</sub>, the linedata in HITRAN2012 terminate  
345 at 1.587 μm, roughly half way through the H<sub>2</sub>S absorption band.

346 Figure 2. Assumed pressure variation of temperature (left-hand panel) and condensible abun-  
347 dances (right-hand panel) assumed in this study for Uranus. The temperature-pressure profile is  
348 based on the ‘F1’ profile<sup>3</sup>. The vertical variation of the CH<sub>4</sub> abundance is as described in the text.  
349 The abundances of NH<sub>3</sub> and H<sub>2</sub>S have simply been limited by their saturation vapour pressures.

350 Figure 3. Fits to average Gemini/NIFS observation of Uranus, made on 2nd November 2010  
351 at 15.3° N, using three different assumptions for the *a priori* imaginary refractive index spectrum,  
352 and excluding H<sub>2</sub>S and NH<sub>3</sub> absorption. The red lines shows the results using  $n_i = 0.001 \pm 0.0005$ ,  
353 the black lines shows the results using  $n_i = 0.01 \pm 0.005$ , while the blue lines show the results  
354 using  $n_i = 0.1 \pm 0.05$ . Panel a) shows the fits to the measured spectra, panel b) shows the difference  
355 between the observed and modelled spectra. Panel c) shows the fitted imaginary refractive index  
356 spectra of the one type of particle assumed right hand plot, while panel d) shows the fitted cloud  
357 profiles (opacity/bar at 1.6  $\mu\text{m}$ ). In panels c) and d) the *a priori* value and range is marked in light  
358 grey, while the error range on the retrieved quantities is indicated in darker grey. The  $\chi^2/n$  of the  
359 fits is also shown in panel a).

360 Figure 4. Fits to the co-added Gemini/NIFS observation of Uranus in the wavelength range  
361 1.56 – 1.6  $\mu\text{m}$ . In the top plot, the observed reflectivity spectrum and estimated error is shown  
362 in grey, the fitted spectrum when H<sub>2</sub>S absorption is not included is shown in red, while the fitted  
363 spectrum when H<sub>2</sub>S absorption is included is shown in black. The bottom plot shows the differ-  
364 ences between these fits and the observed spectrum using the same colours (i.e. red when H<sub>2</sub>S  
365 absorption is not included and black when it is), with the error range again shown in grey. The

366 blue line in the bottom plot shows how the calculated spectrum for the fit when H<sub>2</sub>S absorption is  
367 not included (i.e. red line in the top plot) changes when H<sub>2</sub>S absorption is added (leaving all other  
368 fitted parameters unchanged), assuming a profile with 100% relative humidity (RH). The cyan line  
369 shows how the calculated spectrum changes when NH<sub>3</sub> absorption is added, leaving all other fitted  
370 parameters unchanged, assuming a profile with 1000 times the *a priori* NH<sub>3</sub> profile with 100%  
371 RH.

## 372 **Methods**

373 **Spectral Data Sources** The main gaseous absorber in the H-band (1.4 – 1.8  $\mu\text{m}$ ) in Uranus' spec-  
374 trum is methane. The best available source of methane line data at low temperature in this range is  
375 the WKLMC@80K+<sup>14</sup> line database, which contains the positions, strengths, lower-state energies  
376 and empirical estimates of the rotational quantum number  $J$ , of lines measured at 80K and 296K.  
377 These lines are improved over the WKMC@80<sup>27</sup> database, previously used to analyse the Gem-  
378 ini/NIFS observations reanalysed here for Uranus<sup>2</sup> as they include extra lines that were detected at  
379 296K, but not at 80K, and we have further improved our assignment of line widths, as described  
380 below. For the lines detected at 296K, but not 80K, lower state energies were defined so as to yield  
381 an intensity at 80 K just below the measurement sensitivity threshold. Hence, the contribution of  
382 these lines at cold temperatures bears significant uncertainty. For the lines detected at 80K, but not  
383 296 K, the lower state energies were arbitrarily set to  $-1.0 \text{ cm}^{-1}$ . These line data were converted  
384 to HITRAN format, using the listed strengths at 296 K directly for lines observed at both 80 K and  
385 296 K, and for lines observed only at 80K, we extrapolated their strengths to 296 K using the listed

386 arbitrary lower state energy of  $-1.0 \text{ cm}^{-1}$  and total partition function (rotational + vibrational)  
387 provided as part of HITRAN2012<sup>15</sup>. The spectral range covered by these data is 5852 – 7919  
388  $\text{cm}^{-1}$  (1.262 – 1.709  $\mu\text{m}$ ). These measurements were made for “natural” methane gas, for which  
389 the  $\text{CH}_3\text{D}/\text{CH}_4$  ratio is estimated<sup>14</sup> to be  $5 \times 10^{-4}$ . This is not suitable for calculations in Uranus’  
390 atmosphere, for which the most precise estimate<sup>28</sup> of  $\text{CH}_3\text{D}/\text{CH}_4$  is  $(2.96_{-0.64}^{+0.71}) \times 10^{-4}$  (using an  
391 isotopic enrichment factor<sup>29</sup> of  $f = 1.68 \pm 0.23$ ). Hence, lines for  $\text{CH}_3\text{D}$  were scaled in strength  
392 by 2.96/5. For the foreign-broadened line widths, we used  $J$ -dependent  $\text{H}_2$ - and He-broadened  
393 widths<sup>30</sup>, to which we fitted a 4th-order polynomial in  $J$ , using the widths calculated for  $J = 13$   
394 for higher values of  $J$  to prevent inaccurate extrapolation<sup>31,32</sup>. We assumed temperature depen-  
395 dence coefficients of these foreign-broadened widths for  $\text{H}_2$ -broadening<sup>33</sup> and He-broadening<sup>35</sup>.  
396 For the line shape, we used a Voigt function, but with sub-Lorentzian correction far from line cen-  
397 tre as recommended for  $\text{H}_2$ -broadening conditions<sup>36</sup>. However, we also tested the sub-Lorentzian  
398 corrections suggested for Titan spectra<sup>37</sup> and a sub-Lorentzian correction previously suggested for  
399 modelling Uranus spectra<sup>38</sup>. Using these three different line shapes we took account of all lines  
400 within  $250 \text{ cm}^{-1}$  of each calculation wavelength.

401 Spectroscopic line data for hydrogen sulphide ( $\text{H}_2\text{S}$ ) and ammonia ( $\text{NH}_3$ ) were taken from  
402 HITRAN2012<sup>15</sup>. The line widths and their temperature exponents were also taken from the foreign-  
403 broadened data listed in HITRAN2012. For  $\text{H}_2\text{S}$  these are  $\gamma_{air} = 0.074 \text{ cm}^{-1} \text{ atm}^{-1}$  and a tem-  
404 perature exponent of 0.75, for all lines. HITRAN2012 note that detailed laboratory investigations  
405 are needed to characterise how the line widths vary with the ro-vibrational quantum number, and  
406 there appears to be no published evidence on the appropriate values for an  $\text{H}_2/\text{He}$ -broadening

407 atmosphere. Similarly, for  $\text{NH}_3$ , we used the published HITRAN2012 foreign-broadening pa-  
408 rameters. If the absorption of  $\text{NH}_3$  had proved to be significant, we might have attempted to  
409 use line-broadening parameters more suited to  $\text{H}_2/\text{He}$ -broadening conditions. However, as re-  
410 ported in our paper, the absorption of  $\text{NH}_3$  was not detected in these observations and hence there  
411 was no error introduced by using the listed HITRAN2012 air-broadened widths. We also exam-  
412 ined using ExoMOL line data for  $\text{H}_2\text{S}$ <sup>39</sup> and found negligible differences in the spectra computed  
413 at Gemini/NIFS resolution with the HITRAN2012 line data. Since the HITRAN2012 line data  
414 are much easier to handle (they contain far fewer ‘hot lines’, which are only relevant for high-  
415 temperature calculations) and probably have better constrained line frequencies, we decided to use  
416 HITRAN2012 for both  $\text{NH}_3$  and  $\text{H}_2\text{S}$  line data. In both cases, in the absence of any better informa-  
417 tion and in the expectation of weak absorptions (for which the exact line widths are less important),  
418 we used the published HITRAN2012 air-broadened widths and a Voigt line shape, with a line wing  
419 cut-off of  $35 \text{ cm}^{-1}$  to account for typical sub-Lorentzian wing corrections.

420 The line data were converted to k-distribution look-up tables, or k-tables, covering the Gem-  
421 ini/NIFS H-band spectral range, with 20 g-ordinates, 15 pressures, equally spaced in log pressure  
422 between  $10^{-4}$  and 10 bar, and 14 temperatures, equally spaced between 50 and 180 K. These tables  
423 were precomputed with the modelled instrument line shape of the Gemini/NIFS observations, set  
424 to be Gaussian with a full-width-half-maximum (FWHM) of  $0.0003 \mu\text{m}$ , after an analysis of ARC  
425 lamp calibration spectra<sup>2</sup>.

426 **Observations and wavelength calibration** Observations of Uranus were made with Gemini-  
427 North’s Near-infrared Integral Field Spectrometer (NIFS) instrument in September 2009 and Octo-

ber/November 2010<sup>16,17</sup>, with adaptive optics using Uranus’ nearby moons for wavefront sensing  
(e.g. Ariel, Titania). NIFS’ H-band spectral resolution gives a Gaussian instrument function with  
spectral resolution of  $\text{FWHM} = 0.0003 \mu\text{m}$ . The wavelength calibration provided by the standard  
pipeline of Gemini/NIFS was found to be not quite accurate enough to match the spectral features  
observed here. The assumed wavelength of sample  $i$  in the spectrum is set to  $\lambda_i = \lambda_0 + (i - i_0)\lambda_1$   
, where  $i_0$  is the sample number of the ‘central’ wavelength, and the wavelength centre and step  
were initially assumed to be  $\lambda_0 = 1.55 \mu\text{m}$  and  $\lambda_1 = 0.000155 \mu\text{m}$ , respectively. By comparing  
the measured spectrum to our initial fitted spectrum we found that we could achieve a much better  
fit by modifying these values to  $\lambda_0 = 1.54995 \mu\text{m}$  and  $\lambda_1 = 0.00016036 \mu\text{m}$ . We used these values  
in the subsequent analysis.

**Uranus vertical profiles of temperature and gaseous abundance** The reference temperature  
and abundance profile used in this study (Fig. 2) is based on the ‘F1’ STIS/Voyager-2 profile<sup>3</sup>.  
This profile has a deep methane mole fraction of 4%<sup>19</sup>, and has a varying relative humidity with  
height above the condensation level. The He:H<sub>2</sub> ratio in this profile is set to 0.131 and the profile  
includes 0.04% mole fraction of Ne. To this profile we added abundance profiles of NH<sub>3</sub> and H<sub>2</sub>S,  
assuming arbitrary ‘deep’ mole fractions (i.e. above the putative NH<sub>4</sub>SH cloud) of 0.001 for both,  
and limited their abundance to not exceed the saturated vapour pressure in the troposphere as the  
temperature falls with height. As the abundances of these gases (and CH<sub>4</sub>) decrease with pressure  
the abundance of H<sub>2</sub> and He is adjusted to ensure the sum of mole fractions adds to unity (keeping  
He:H<sub>2</sub> = 0.131, or equivalently 12:88); the heights are calculated from the hydrostatic equation  
using the local temperature, gravitational acceleration and local mean total molecular weight.

449 For comparison we also performed retrievals using the temperature-pressure profile deter-  
450 mined from Spitzer observations of Uranus' mid-IR spectrum<sup>24</sup>, again with 'deep' NH<sub>3</sub> and H<sub>2</sub>S  
451 abundances of 0.001. H<sub>2</sub> and He were assumed to be present with a ratio 85:15, again ensuring the  
452 sum of mole fractions adds to unity at all heights.

453 **Radiative-transfer analysis** The vertical cloud structure was retrieved from the Gemini/NIFS ob-  
454 servations using the NEMESIS<sup>18</sup> radiative-transfer and retrieval code. NEMESIS models planetary  
455 spectra either using a line-by-line model, or by using the correlated-k approximation<sup>40</sup>. For speed,  
456 these retrievals were conducted using the method of correlated-k, but we regularly checked that  
457 we obtained the same model spectra (to within error) using a line-by-line approach. To model  
458 these reflected-sunlight spectra, a matrix-operator multiple-scattering model<sup>41</sup> was used, with 5  
459 zenith angles (i.e. 5 upwards and 5 downwards) and the number of required components in the  
460 Fourier azimuth decomposition determined from the maximum of the reflected or incident-solar  
461 zenith angles. The collision-induced absorption of H<sub>2</sub>-H<sub>2</sub> and H<sub>2</sub>-He was modelled with published  
462 coefficients<sup>42-44</sup>. Rayleigh scattering was also included for completeness, but was found to be  
463 negligible at these wavelengths.

464 To analyse the measured radiance spectra within our radiative transfer model we initially  
465 used the high-resolution 'CAVIAR' solar spectrum<sup>45</sup>, which we smoothed to the NIFS resolution of  
466  $\Delta\lambda = 0.0003\mu\text{m}$ . However, we found that this spectrum (and others, e.g.<sup>46,47</sup>) contained spurious  
467 'Fraunhofer lines' that did not seem to correspond to features seen at these wavelengths in the  
468 Uranus spectra. We must assume that the method used to generate these 'Extraterrestrial Solar  
469 Spectra' (ESS), namely measuring the solar spectrum at the ground at various zenith angles and

470 extrapolating to an airmass of zero, leads to small errors at these wavelengths. Hence, we used  
471 a smoothed version of the solar spectrum<sup>47</sup> in our calculations, omitting the spurious ‘Fraunhofer  
472 lines’, which we found matched our observations much more closely.

473 The observed spectrum (with  $n_y = 937$  spectral points) was fitted with NEMESIS using a  
474 continuous distribution of cloud particles whose opacity at 39 levels spaced between  $\sim 10$  and  
475  $\sim 0.01$  bar was retrieved. For this cloud profile the *a priori* opacity values (at  $1.6 \mu\text{m}$ ) were set to  
476  $0.001 \pm 0.0005 \text{ g}^{-1} \text{ cm}^2$  at all levels (equating to opacity/bar values of  $\sim 1$ ), with a ‘correlation  
477 length’ of 1.5 scale heights to ensure the profile was vertically smooth. NEMESIS treats cloud  
478 opacity as log values and so the error was converted to  $\pm 50\%$ . The particles were assumed to have  
479 a standard Gamma size distribution with mean radius  $1.0 \mu\text{m}$  and variance 0.05, which are typical  
480 values assumed in previous analyses. Using a previously published technique<sup>21</sup>, NEMESIS was  
481 used to retrieve the imaginary refractive index spectrum of these particles. The *a priori* imaginary  
482 refractive index spectrum was sampled at every  $0.05 \mu\text{m}$  between  $1.4$  and  $1.8 \mu\text{m}$ , with a ‘cor-  
483 relation length’ of  $0.1 \mu\text{m}$  set in the covariance matrix, to ensure that retrieved spectrum varied  
484 reasonably smoothly with wavelength. At each iteration of the model, the real part of the parti-  
485 cles’ refractive index spectrum was computed from the imaginary part using the Kramers-Kronig  
486 relation<sup>48</sup>, fixing the real part of the refractive index of these particles to 1.4 at a wavelength of  
487  $1.6 \mu\text{m}$ . Self-consistent scattering properties were then calculated using Mie theory, but the Mie-  
488 calculated phase functions were approximated with combined Henyey-Greenstein functions at each  
489 wavelength to smooth-over features peculiar to perfectly spherical scatterers such as the ‘rainbow’  
490 and ‘glory’. This is justified since we expect the actual aerosols in the atmosphere of Uranus to

491 be solid condensates, and thus non-spherical. However, assuming these non-spherical particles  
492 are randomly orientated with respect to each other, the bulk scattering properties, such as cross-  
493 section and single-scattering albedo, are reasonably approximated with Mie theory<sup>34</sup>, especially if  
494 the phase functions are also modified as we describe.

495         Since methane is the main gaseous absorber we tested to see whether some of the approx-  
496 imations assumed in the WKLMC@80K+<sup>14</sup> line database might be having an adverse effect on  
497 our calculations. We first checked whether excluding the lines observed at 296 K, but not at 80  
498 K (and which are assigned a lower state energy high enough to reduce the computed strength at  
499 80 K to be below the measurement noise limit) might significantly affect the calculated spectra,  
500 but found very little difference when these lines were neglected. We also checked the effect ex-  
501 cluding the lines observed only at 80 K as well (and which are assigned an arbitrary lower state  
502 energy of  $-1 \text{ cm}^{-1}$ ). In this case, the differences were larger, but on the whole the model correctly  
503 reproduced the shape and main features of the observed spectrum.

504 **Retrieval Tests** Supplementary Fig. 12 shows our fit to the Uranus spectrum, setting the *a pri-*  
505 *ori* imaginary refractive indices to  $0.01 \pm 0.005$  at all wavelengths and using the three different  
506 sub-Lorentzian line shapes for  $\text{CH}_4$  (neglecting  $\text{H}_2\text{S}$  and  $\text{NH}_3$  absorption). We found that each  
507 assumption for the sub-Lorentzian correction gave a very similar fit to the spectrum ( $\chi^2/n \sim$   
508 1.7–1.9), which was initially puzzling. However, the reason for this is easy to understand from  
509 Supplementary Fig. 12. The effect of different sub-Lorentzian corrections is most apparent on the  
510 shortwave side of the strong absorption band at  $1.7 - 1.8 \mu\text{m}$  and previous studies have tuned the  
511 correction to get the best match to the observed spectrum between  $1.5$  and  $1.62 \mu\text{m}$ . Our current

512 model, however, can very easily fit this region by varying the imaginary refractive index spectrum  
513 of the particles and it can be seen that very different imaginary refractive index spectra are retrieved  
514 for the three different sub-Lorentzian corrections, but very similar vertical cloud distributions and  
515 similar spectral fits. In other words, there is a degeneracy between the sub-Lorentzian corrections  
516 and the retrieved imaginary refractive index. In fact, we had to be careful not to allow the imagi-  
517 nary refractive index retrieval too much freedom. Early retrievals sampled the imaginary refractive  
518 index spectrum more finely ( $\Delta\lambda = 0.005\mu\text{m}$ ) over the  $1.56 - 1.6 \mu\text{m}$  range and significant part  
519 of the spectral variation of reflectivity was accounted for by variations in  $n_i$ , which it was difficult  
520 to justify as being realistic. We thus assumed the slow wavelength-to-wavelength variation in  $n_i$   
521 as described. Since the line shape recommended for H<sub>2</sub>-He atmospheres<sup>36</sup> gave a good fit to the  
522 observations, we chose to use this assumption in our final analysis.

523 **Scattering Properties** Since the fitted imaginary refractive index spectrum for our cloud particles  
524 has values of typically  $n_i \sim 0.06$ , this leads the particles to be quite absorbing. This can best be  
525 seen in Supplementary Fig. 1, where we compare the computed wavelength dependence of the  
526 extinction cross-section (normalised to  $1.6 \mu\text{m}$ ), the single-scattering albedo, and the asymmetry,  
527  $g$ , of the forward part of the fitted combined Henyey-Greenstein phase functions for the case when  
528 the *a priori* imaginary refractive indices were set to  $0.01 \pm 0.005$ . We found the back-scattering  
529 part of the phase-function to be insignificant. As we can see the single-scattering albedo has values  
530 of  $\varpi = 0.7 - 0.8$ , while the phase function asymmetry,  $g$ , is  $\sim 0.7$ .

531 **3 Data availability statement**

532 The data that support the plots within this paper and other findings of this study are available from  
533 the corresponding author upon reasonable request.

534 **4 Methods References**

535 27. Campargue, A., Wang, L., Mondelain, D., Kassi, S., Bézard, B., Lellouch, E., Coustenis, A.,  
536 de Bergh, C., Hirtzig, M. & Drossart, P. An empirical line list for methane in the 1.26 – 1.71  
537  $\mu\text{m}$  region for planetary investigations (T = 80 – 300 K). Application to Titan. *Icarus* **219**, 110  
538 –128 (2012).

540 28. Feuchtgruber, H., Lellouch, E., Orton, G., de Graauw, T., Vandenbussche, B., Swinyard, B.,  
541 Moreno, R., Jarchow, C., Billebaud, F., Cavalié, T., Sidher, S. & Hartogh, P. The D/H ratio in  
542 the atmospheres of Uranus and Neptune from Herschel-PACS observations. *Astron. Astrophys.*  
543 **551**, A126 (2013).

544 29. Lécluse, C., Robert, F., Gautier, D. & Guiraud, M. Deuterium enrichment in giant planets.  
545 *Planet. Space Sci.* **44**, 1579 – 1592 (1996).

546 30. Pine A. S. Self-, N<sub>2</sub>-, O<sub>2</sub>-, H<sub>2</sub>-, Ar-, and He- broadening in the  $\nu_3$  band Q branch of CH<sub>4</sub>. *J.*  
547 *Chem. Physics* **97**, 773 – 785 (1992).

548 31. Amundsen D. S., Baraffe I., Tremblin P., Manners J., Hayek W., Mayne N. J. & Acreman D.  
549 M. Accuracy tests of radiation schemes used in hot Jupiter global circulation models. *Astron.*

- 550 *Astrophys.* **564**, A59 (2014).
- 551 32. Garland, R. & Irwin, P.G.J., 2018. Effectively calculating gaseous absorption in radiative  
552 transfer models of exoplanetary and brown dwarf atmospheres. *Mon. Not. R. Astro. Soc.* (in  
553 preparation, 2018).
- 554 33. Margolis J. S. Hydrogen broadening and collision-induced line shifts of methane at 4200  
555  $\text{cm}^{-1}$ . *J.Q.S.R.T.* **49**, 71 – 79 (1993).
- 556 34. Mishchenko M. I., Travis, L. D., Khan, R.A. & West, R. A. Modeling phase functions for dust-  
557 like tropospheric aerosols using a shape mixture of randomly oriented polydisperse spheroids.  
558 *J. Geophys. Res.* **102**, 16831 – 16847 (1997).
- 559 35. Varanasi P. & Chudamani S. The temperature dependence of lineshifts, linewidths and line  
560 intensities of methane at low temperatures. *J.Q.S.R.T.* **43**, 1 – 11 (1990).
- 561 36. Hartmann, J.-M., Boulet, C., Brodbeck, C., van Thanh, N., Fouchet, T. & Drossart, P. A far  
562 wing lineshape for H<sub>2</sub>-broadened CH<sub>4</sub> infrared transitions. *J.Q.S.R.T.* **72**, 117 – 122 (2002).
- 563 37. de Bergh, C., Courtin, R., Bézard, B., Coustenis, A., Lellouch, E., Hirtzig, M., Rannou, P.,  
564 Drossart, P., Campargue, A., Kassi, S., Wang, L., Boudon, V., Nikitin, A. & Tyuterev, V.  
565 Applications of a new set of methane line parameters to the modeling of Titan's spectrum in  
566 the 1.58  $\mu\text{m}$  window. *Planet. Space Sci.* **61**, 85 – 98 (2012).
- 567 38. L.A. Sromovsky, Fry, P.M., Boudon, V., Campargue, A. & Nikitin, A. Comparison of line-  
568 by-line and band models of near-IR methane absorption applied to outer planet atmospheres.  
569 *Icarus* **218**, 1 – 23 (2012).

- 570 39. Azzam, A. A. A., Tennyson, J., Yurchenko, S. N. & Naumenko, O. V. ExoMol molecular line  
571 lists - XVI: The rotation-vibration spectrum of hot H<sub>2</sub>S. *Mon. Not. Roy. Ast. Soc.* **460**, 4063 –  
572 4074 (2016).
- 573 40. Lacis, A.A. & Oinas, V. A description of the correlated-k distribution method for modelling  
574 nongray gaseous absorption, thermal emission, and multiple scattering in vertically inhomo-  
575 geneous atmospheres. *J. Geophys. Res.* **96**, 9027 – 9063 (1991).
- 576 41. Plass, G.N., Kattawar, G.W. & Catchings, F.E. Matrix operator method of radiative transfer.  
577 1: Rayleigh scattering. *Appl. Opt.* **12**, 314 – 329 (1973).
- 578 42. Borysow, A. Modeling of collision-induced infrared absorption spectra of H<sub>2</sub> – H<sub>2</sub> pairs in the  
579 fundamental band at temperatures from 20 to 300 K. *Icarus* **92**, 273 – 279 (1991).
- 580 43. Borysow, A. New model of collision-induced infrared absorption spectra of H<sub>2</sub> – He pairs in  
581 the 2 – 2.5 μm range at temperatures from 20 to 300 K – An update. *Icarus* **96**, 169 – 175  
582 (1992).
- 583 44. Zheng, C. & Borysow, A. Modeling of collision-induced infrared absorption spectra of H<sub>2</sub>  
584 pairs in the first overtone band at temperatures from 20 to 500 K. *Icarus* **113**, 84 – 90 (1995).
- 585 45. Menang, K.P., Coleman, M.D., Gardiner, T.D., Ptashnik, I.V. & Shine, K.P. A high-resolution  
586 near-infrared extraterrestrial solar spectrum derived from ground-based Fourier transform  
587 spectrometer measurements. *J. Geophys. Res.* **118**, 5319 – 5331 (2013).
- 588 46. Fiorenza, C. & Formisano, V. A solar spectrum for PFS data analysis. *Planet. Space Sci.* **53**,  
589 1009 – 1016 (2005).

- 590 47. Thuillier, G., Hersé, M., Labs, D., Foujols, T., Peetermans, W., Gillotay, D., Simon, P.C. &  
591 Mandel, H. The solar spectral irradiance from 200 to 2400 nm as measured by the SOLSPEC  
592 spectrometer from the ATLAS and EURECA missions. *Solar Physics* **214**, 1 – 22 (2003).
- 593 48. Sheik-Bahae. Nonlinear Optics Basics. Kramers-Kronig Relations in Nonlinear Optics. In  
594 Robert D. Guenther. *Encyclopedia of Modern Optics*. Amsterdam: Academic Press (2005).

Table 1: Retrieval results at all areas considered on Uranus' disc.

Area	Latitude	$p_1$	$f_{H_2S}$	$\chi^2/n$	$\chi^2/n_y$	$\Delta\chi^2$	$x_{H_2S}$	$A_{H_2S}$	$R_H$
1 <sup>a</sup>	15.3°N	1.99	113 ± 12	1.30	1.23	367.3	0.47	2.7	2.1
2	13.8°N	2.00	134 ± 19	1.04	0.99	140.7	0.58	3.3	2.3
3	15.3°S	2.10	123 ± 16	1.23	1.17	225.1	0.80	4.9	2.5
4	32.5°N	1.88	303 ± 45	1.31	1.24	218.7	0.82	4.4	2.6
5	44.7°N	1.66	474 ± 84	1.33	1.26	172.9	0.43	2.1	2.8
6 <sup>b</sup>	62.0°N	1.56	252 ± 211	1.31	1.24	1.8	0.13	0.6	3.9
7	4.9°N	1.98	96 ± 9	1.57	1.48	333.8	0.38	2.2	2.2
1 <sup>c</sup>	15.3°N	2.28	16 ± 2	1.36	1.29	292.1	0.43	2.9	2.1

Notes:  $p_1$  is the pressure(bar) where the cloud opacity to space is unity;  $f_{H_2S}$  is the retrieved H<sub>2</sub>S relative humidity (%);  $\chi^2/n$  is the reduced chi-squared statistic of the fit when H<sub>2</sub>S is included, where  $n = n_y - n_x = 889$ ;  $\chi^2/n_y$  is the chi-squared statistic of the fit when H<sub>2</sub>S is included, where  $n_y = 937$ ;  $\Delta\chi^2$  is how much the  $\chi^2$  of the fit reduces when H<sub>2</sub>S absorption is included – values greater than 9 can be considered significant;  $x_{H_2S}$  is mole fraction of H<sub>2</sub>S (ppm) at  $p_1$ ;  $A_{H_2S}$  is the column amount of H<sub>2</sub>S (10<sup>19</sup> molecule cm<sup>-2</sup>) above  $p_1$ ;  $R_H$  is a haze 'index' – the ratio of the average radiance from 1.63 – 1.64  $\mu$ m divided by the average radiance from 1.57 – 1.58  $\mu$ m, expressed as %.

Further notes: <sup>a</sup>Area 1 is the main area studied; <sup>b</sup>For polar area 6, where the radiance is lower, the measurement errors did not need to be multiplied by 1.6 ensure a good  $\chi^2/n$ ; <sup>c</sup>Same area as reference, but analysed using the Spitzer temperature profile, rather than 'F1'.

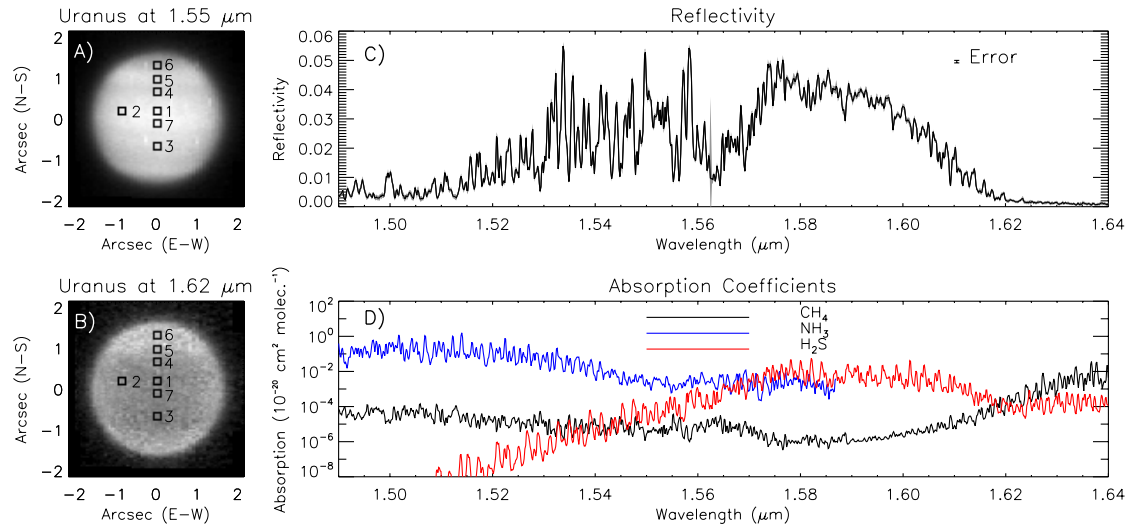


Figure 1: The appearance and spectrum of Uranus at the near-infrared wavelengths observed by Gemini/NIFS and associated absorption spectra of  $\text{CH}_4$ ,  $\text{NH}_3$  and  $\text{H}_2\text{S}$ . Panel A: The appearance of Uranus at  $1.55 \mu\text{m}$  (low methane absorption, showing reflection for cloud/haze at all vertical levels), observed with Gemini/NIFS on 2nd November 2010 at approximately 06:00UT, showing the position of the seven  $5 \times 5$  pixel test areas picked for retrieval analysis. Panel B: The appearance of Uranus at  $1.62 \mu\text{m}$  (high methane absorption, showing reflection from upper atmospheric haze only). Panel C: Reference spectrum of Uranus<sup>16</sup> analysed in this study, averaged over area '1' just north of the equator, near the disc centre, with a mean latitude of  $15.3^\circ\text{N}$ , and error estimates shown in grey. Panel D: Mean strength listed in the k-distribution tables used in this study across the Gemini/NIFS spectral range. These absorption tables were generated from the WKL $\text{MC@80K+}$ <sup>14</sup> database for  $\text{CH}_4$ , and from HITRAN2012<sup>15</sup> for  $\text{H}_2\text{S}$  and  $\text{NH}_3$ . These mean absorption coefficients have been computed at a temperature of 100 K and pressure of 1 atm, similar to conditions found at the tops of Uranus' main visible clouds. Note that for  $\text{NH}_3$ , the linedata in HITRAN2012 terminate at  $1.587 \mu\text{m}$ , roughly half way through the  $\text{H}_2\text{S}$  absorption band.

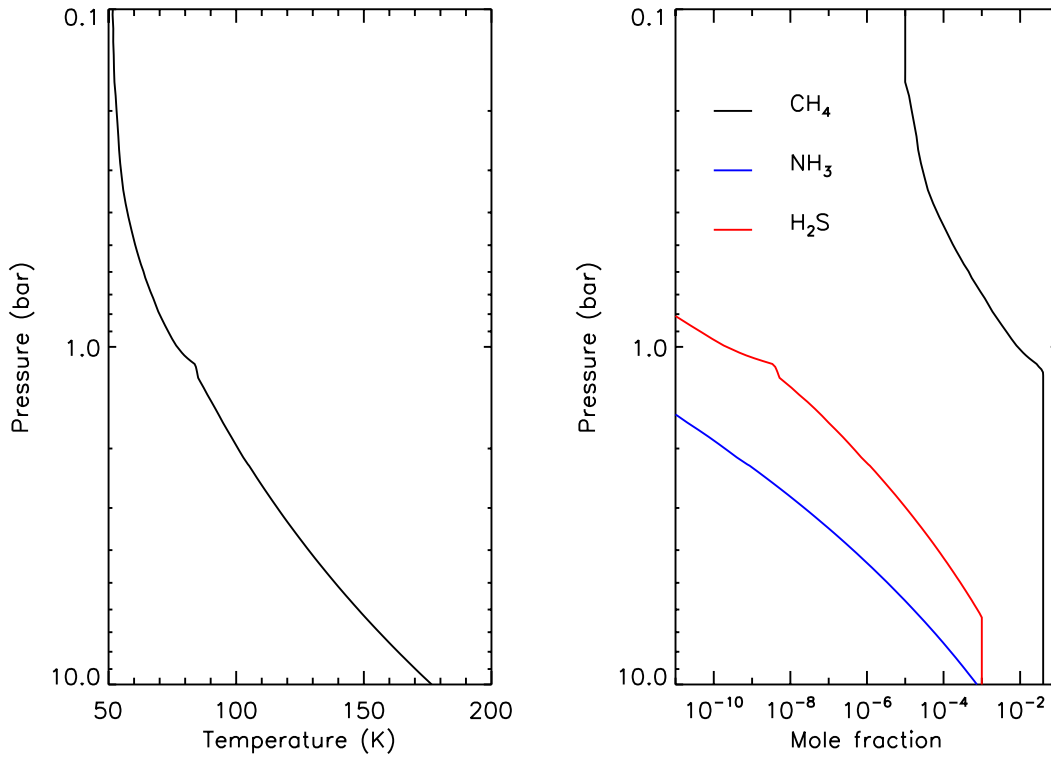


Figure 2: Assumed pressure variation of temperature (left-hand panel) and condensible abundances (right-hand panel) assumed in this study for Uranus. The temperature-pressure profile is based on the ‘F1’ profile<sup>3</sup>. The vertical variation of the  $\text{CH}_4$  abundance is as described in the text. The abundances of  $\text{NH}_3$  and  $\text{H}_2\text{S}$  have simply been limited by their saturation vapour pressures.

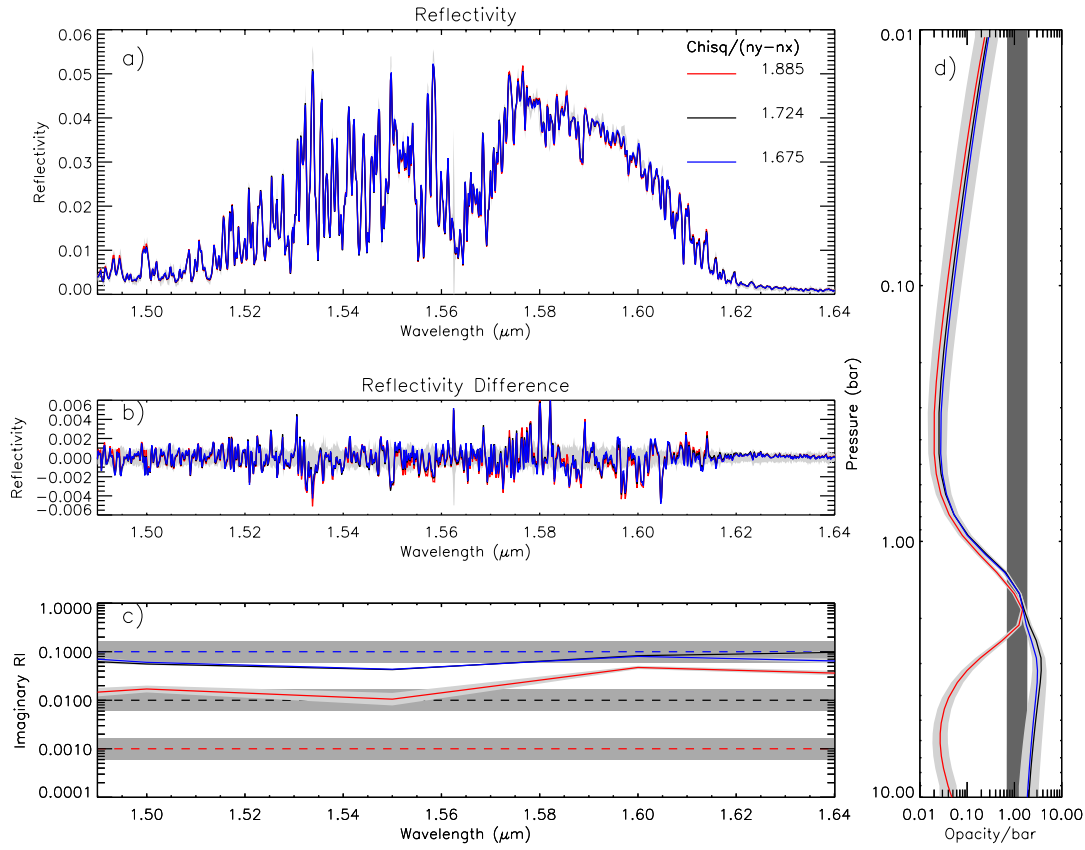


Figure 3: Fits to average Gemini/NIFS observation of Uranus, made on 2nd November 2010 at  $15.3^\circ$  N, using three different assumptions for the *a priori* imaginary refractive index spectrum, and excluding  $\text{H}_2\text{S}$  and  $\text{NH}_3$  absorption. The red lines shows the results using  $n_i = 0.001 \pm 0.0005$ , the black lines shows the results using  $n_i = 0.01 \pm 0.005$ , while the blue lines show the results using  $n_i = 0.1 \pm 0.05$ . Panel a) shows the fits to the measured spectra, panel b) shows the difference between the observed and modelled spectra. Panel c) shows the fitted imaginary refractive index spectra of the one type of particle assumed right hand plot, while panel d) shows the fitted cloud profiles (opacity/bar at  $1.6 \mu\text{m}$ ). In panels c) and d) the *a priori* value and range is marked in light grey, while the error range on the retrieved quantities is indicated in darker grey. The  $\chi^2/n$  of the fits is also shown in panel a).

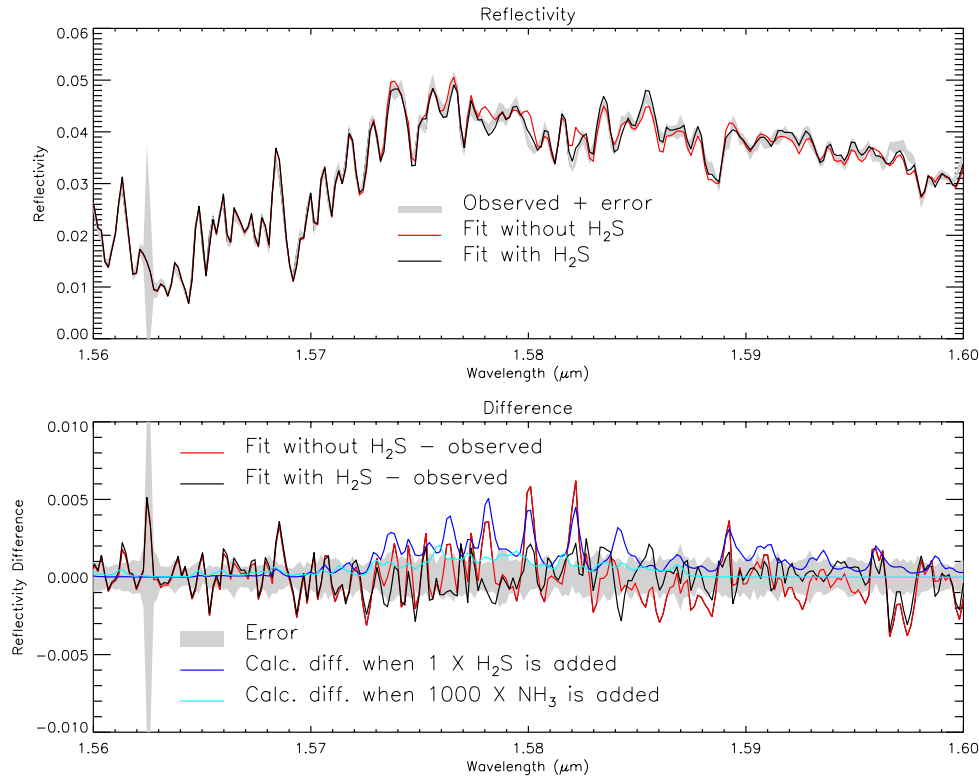


Figure 4: Fits to the co-added Gemini/NIFS observation of Uranus in the wavelength range 1.56 – 1.6  $\mu\text{m}$ . In the top plot, the observed reflectivity spectrum and estimated error is shown in grey, the fitted spectrum when  $\text{H}_2\text{S}$  absorption is not included is shown in red, while the fitted spectrum when  $\text{H}_2\text{S}$  absorption is included is shown in black. The bottom plot shows the differences between these fits and the observed spectrum using the same colours (i.e. red when  $\text{H}_2\text{S}$  absorption is not included and black when it is), with the error range again shown in grey. The blue line in the bottom plot shows how the calculated spectrum for the fit when  $\text{H}_2\text{S}$  absorption is not included (i.e. red line in the top plot) changes when  $\text{H}_2\text{S}$  absorption is added (leaving all other fitted parameters unchanged), assuming a profile with 100% relative humidity (RH). The cyan line shows how the calculated spectrum changes when  $\text{NH}_3$  absorption is added, leaving all other fitted parameters unchanged, assuming a profile with 1000 times the *a priori*  $\text{NH}_3$  profile with 100% RH.